


Contact-angle-hysteresis effects on a drop sitting on an incline plane

Pablo D. Ravazzoli, Ingrith Cuellar, Alejandro G. González, and Javier A. Diez
*Instituto de Física Arroyo Seco, Universidad Nacional del Centro de la Provincia de Buenos Aires,
 and CIFICEN-CONICET-CICPBA, Pinto 399, 7000 Tandil, Argentina*

 (Received 1 October 2018; revised manuscript received 20 February 2019; published 16 April 2019)

We study the contact-angle hysteresis and morphology changes of a liquid drop sitting on a solid substrate inclined with respect to the horizontal at an angle α . This one is always smaller than the critical angle, α_{crit} , above which the drop would start to slide down. The hysteresis cycle is performed for positive and negative α 's ($|\alpha| < \alpha_{\text{crit}}$), and a complete study of the changes in contact angles, free surface, and footprint shape is carried out. The drop shape is analyzed in terms of a solution of the equilibrium pressure equation within the long-wave model (lubrication approximation). We obtain a truncated analytical solution describing the static drop shapes that is successfully compared with experimental data. This solution is of practical interest since it allows for a complete description of all the drop features, such as its footprint shape or contact angle distribution around the drop periphery, starting from a very small set of relatively easy to measure drop parameters.

DOI: [10.1103/PhysRevE.99.043105](https://doi.org/10.1103/PhysRevE.99.043105)

I. INTRODUCTION

The problem of a sessile drop sitting on an incline has been the subject of numerous investigations in the past three decades. Some of them have been concerned with the relationship between the maximum plane inclination above which the drop slides down, α_{crit} , and the parameters characterizing the initial conditions [1–4]. Many studies aim to describe the retention forces needed to achieve this critical inclination angle [5–9], while other related works focus on the dynamics of droplets sliding down an incline [10,11].

An aspect that has drawn considerable attention in this context is the shape that a tilted sessile drop adopts under different plane inclinations, α (see Fig. 1). This problem can be theoretically tackled by means of two equivalent approaches, namely the equilibrium of pressures (by using the Young-Laplace equation) or the energy minimization method (by considering both surface and gravitational energies in an Euler-Lagrange framework). The latter has been considered by using different assumptions, e.g., that footprints remains circular for $\alpha \neq 0$ [12–15]. However, there is experimental evidence that the drop footprints on inclines are not circular. Therefore, some authors have proposed alternative noncircular footprints, such as straight lines and circular endings [1]. Although this shape is very simple and easy to deal with, it does not correspond to observations. A more accurate approximation was developed in [16], where the drop footprint is approximated by two superimposed ellipses sharing a common tangent at the maximum width. However, these proposals are ad hoc and are not based on physical grounds.

The use of the Surface Evolver simulation tool [4,17–19] is able to yield other noncircular footprints. Alternative approaches numerically obtain the footprint shapes considering a hybrid diffuse interface with a smoothed particle hydrodynamics model [20], or an equilibrium variation approach that accounts for a drop's virtual motion on the footprint [21]. The experiments in [22] for a tilted water drop on a siliconized

flat glass slide have shown that there are three transitions of partial depinning, namely that of the advancing and receding parts of the contact line, and that of the entire contact line leading to the drop's translational motion. However, as we will see here, the first two stages do not necessarily occur successively as α increases, but an important overlapping of both stages is possible. Chou *et al.* [17] have compared their theory with the experimental footprints from Ref. [22], and the discrepancies were attributed to the initially noncircular footprint of the experiments. In this work, we will observe that the experiments carried out in [17] correspond only to the initial stages of the complete α -cycles reported here.

The analysis of this deceptively simple problem is very complex since it requires a thorough comprehension of the phenomena related to contact-angle hysteresis. In general, this property has been studied by measuring the contact angle of a sessile drop on a horizontal plane for a given volume, V . This is usually done by injecting and withdrawing liquid with a needle touching the top of the drop (see, e.g., [23]). A recent study [24] has shown that, under volume changes, the drop achieves its equilibrium by adjusting the contact angle, θ , within a given interval with two different contact line behaviors, i.e., it remains pinned or it alternatively depins and stops when reaching a new static state. This latter process is performed by either receding or advancing the contact line in small amounts, δr , from the previous equilibrium. The resulting cycle is depicted in Fig. 2, where Δr indicates the total displacement of the contact line from the initial situation to the other equilibrium state, i.e., Δr is the summation of all δr up to the static state under consideration. Thus, $\Delta r = 0$ corresponds to point O [see also Fig. 2(b) in [24]]. The entrance to the cycle is shown by the path OA along which the drop volume increases while θ remains constant. The right (AB) and bottom (BC) branches result from decreasing volumes ($\Delta V < 0$), while the left (CD) and top (DA) ones correspond to $\Delta V > 0$. The three possible behaviors mentioned above are limited by four characteristic contact angles, which define

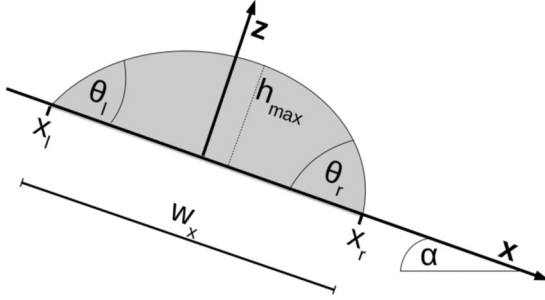


FIG. 1. Sketch of the drop cross section along the symmetry vertical plane on an incline.

the following three stages: (i) the contact line remains pinned for $\theta_{\text{rcd}} < \theta < \theta_{\text{adv}}$, (ii) it recedes and reaches equilibrium for $\theta_{\text{min}} < \theta < \theta_{\text{rcd}}$, and (iii) it advances and reaches equilibrium for $\theta_{\text{adv}} < \theta < \theta_{\text{max}}$. Note that it is usual to define the hysteresis range only by the interval of case (i), where the contact line is pinned. However, other equilibrium solutions are also found out of this range after some contact line displacements, and they exist within the wider interval $(\theta_{\text{min}}, \theta_{\text{max}})$. These θ -values characterize fundamental properties of the hysteresis cycle and do not depend on the volume change, ΔV , while the displacements Δr may change with it.

In this paper, instead of considering the drop volume, V , as the variable parameter for $\alpha = 0$, we vary the inclination angle, α , for a given V . The goal is to show that a similar hysteresis cycle with the same four characteristic angles can be found by means of this alternative procedure. Thus, we wish to confirm that the θ -range of the hysteresis cycle is an intrinsic property of the liquid-solid interaction, no matter which parameter is varied around it, V or α . In particular, we will start the cycle at $\alpha = 0$ and analyze the drop equilibrium states within the interval $(-\alpha_{\text{max}}, \alpha_{\text{max}})$, where $\alpha_{\text{max}} \lesssim \alpha_{\text{crit}}$ (in our case $\alpha_{\text{crit}} \approx 26^\circ$). One advantage of the procedure of changing α for fixed V is that it is not invasive, since the drop is only in contact with the substrate, and no needle is perturbing its free surface. In contrast to the procedure with

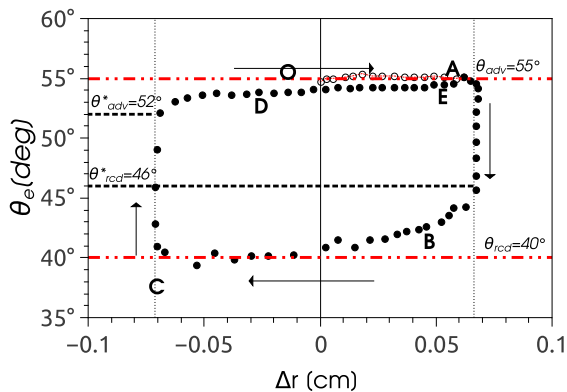


FIG. 2. Scheme of the contact-angle-hysteresis cycle. Point O corresponds to the initial situation where the drop volume is V and $\Delta r = 0$. The line OA shows the path to enter the cycle ABCD. Both V and θ decrease (increase) from A to C (C to A). Note that there is a pinned contact line ($\Delta r = \text{const}$) along AB and CD, while there is depinning along BC and DA [see Fig. 2(b) in [24]].

variable V and $\alpha = 0^\circ$, the axial symmetry is lost, since the drop footprint is no longer circular as the plane is inclined. This seeming drawback is used here to obtain two hysteresis cycles, one for the left and another for the right contact points of the drop when observed laterally. Note that these points change their downhill or uphill character as α changes sign.

Moreover, we are also concerned with the modifications of the drop shape as the inclination varies in the interval $(-\alpha_{\text{max}}, \alpha_{\text{max}})$. In particular, the experiments show an expected symmetry of the profiles for positive and negative values of α , which can be used as an assessment of our experimental accuracy. We also calculate the theoretical drop shape by resorting to a long-wave theory approach that yields a simplified differential equation for drop thickness, h . Within this approximation, known as lubrication theory, we find an analytical solution in the form of a series. To obtain a solution for practical use, we propose a truncated expression, whose coefficients can be calculated from a small set of easily measured drop parameters, namely the drop extensions along both downhill and transverse directions, and the downhill contact angle. Using this model, we are able to predict other measured features of the drop that require more complex diagnostics, such as the uphill contact angle, the maximum drop thickness, and the footprint shape. A comparison is made between these predictions and their measured counterparts.

The paper is organized as follows. Section II describes the experimental setup and presents measured data regarding the whole hysteresis cycle, which can be divided into five main branches. We also analyze the drop thickness profiles by comparing measurements for positive and negative α 's. Then, we describe the formalism to account for the calculation of the equilibrium drop shape in Sec. III. We find the solution of the equations within the lubrication theory, and we use a truncated approximation to obtain the main geometrical features of the drop, which are compared with the experimental data. Finally, Sec. IV is devoted to a summary and conclusions.

II. EXPERIMENTS AND DESCRIPTION OF THE HYSTERESIS CYCLE

The experiments are performed on a substrate that is partially wetted by our working fluid, namely a silicone oil [polydimethylsiloxane (PDMS)]. The substrate is a glass (microscope slide) coated with a fluorinated solution (EGC-1700 of 3M) by controlling both the dip coating velocity (≈ 0.1 cm/min) and the drying time of the solvent solution ($t \approx 30$ min) in an oven at temperature $T \approx 40^\circ\text{C}$. Under this protocol, we ensure that the PDMS partially wets the substrate in a repeatable way, so that a drop of given volume placed on a horizontal substrate always reaches the same contact angle (within an experimental error of $\pm 0.5^\circ$). Surface tension, γ , and density, ρ , of PDMS are measured with a Krüss K11 tensiometer, while its viscosity, μ , is determined with a Haake VT550 rotating viscometer. The values of these parameters are $\gamma = 21$ dyn/cm, $\rho = 0.97$ g/cm³, and $\mu = 21.7$ Poise at temperature $T = 20^\circ\text{C}$.

The same kind of substrate and PDMS were previously used in [24], where the static contact angle, θ , of a single sessile drop with a circular footprint on a horizontal substrate was measured. In that work, we were able to study

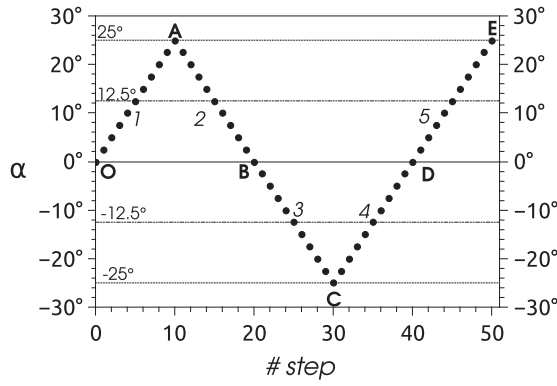


FIG. 3. Inclination angle, α , as a function of the number of steps for $\alpha_{\max} = 25^\circ$. The complete cycle is $0^\circ \rightarrow 25^\circ \rightarrow 0^\circ \rightarrow -25^\circ \rightarrow 0^\circ \rightarrow 25^\circ$. Each step corresponds to $\Delta\alpha = 2.5^\circ$. The numbers and letters indicate the branches and their extreme points, respectively.

the hysteresis cycle of θ by injecting and withdrawing fluid with a needle in contact with the top of the drop. This was done by measuring θ [as well as the thickness profile, $h(x)$] with a Rame-Hart goniometer Model 250. In particular, we found $\theta_{\max} = 55^\circ$ and $\theta_{\min} = 40^\circ$, while the contact angles at which the contact line displaces to achieve equilibrium, that is, the advancing and receding angles, were $\theta_{\text{adv}} = 52^\circ$ and $\theta_{\text{rcd}} = 46^\circ$, respectively.

Unlike the experiments in [24], the goniometer is now mounted on a tilted base with a variable inclination angle, α . Since the goal here is to analyze the deformations of the drop shape due to changes in α , the substrate is inclined in successive steps of $\Delta\alpha = 2.5^\circ$, and we consider the cycle $0^\circ \rightarrow \alpha_{\max} \rightarrow 0^\circ \rightarrow -\alpha_{\max} \rightarrow 0^\circ \rightarrow \alpha_{\max}$, with $\alpha_{\max} < \alpha_{\text{crit}} \approx 26^\circ$ (see Fig. 3). The branches are numbered from 1 to 5, the starting point is denoted by O, and the extreme points by A, B, C, D, and E. We measure the positions of the contact line points on the *right*, x_r , and *left*, x_l , of the drop profile at the xz plane (see Fig. 1) as well as the corresponding contact angles,

θ_r and θ_l . Note that x_r corresponds to the downhill (uphill) point for $\alpha > 0$ ($\alpha < 0$), and vice versa for x_l .

The thickness profiles and footprint shapes at every point of the cycle are obtained from images such as those shown in Fig. 4. The top (bottom) line shows the side (top) views of the drop for $\alpha = 0^\circ, 12.5^\circ$, and 25° . The reflected image of the drop on the substrate, as seen at the top line of the picture, is used to determine the substrate position as well as the segment connecting the side vertices (its length yields the drop extension, w_x). The thick green lines in the top pictures indicate the thickness profiles, while those in the bottom pictures (top views) correspond to the footprint shapes.

The initial contact angle at point O, θ_0 , depends on how the drop is set up on the substrate. For this task, we use an automatic dispenser syringe; thus, θ_0 may result in the range $\theta_{\text{adv}} < \theta_0 < \theta_{\text{max}}$ since the drop reaches equilibrium by spreading after being deposited with the needle. Usually, it turns out to be $\theta_0 = \theta_{\text{max}}$, but it can be reduced a bit if some drop fluid is withdrawn with the needle. In the following, we will analyze the effects of both α_{\max} and θ_0 on the hysteresis cycle.

We start our study with $\alpha_{\max} = 25^\circ$ and $\theta_0 = \theta_{\text{max}} = 55^\circ$. The measured displacements Δx_l and Δx_r (with respect to their positions for $\alpha = 0^\circ$) versus α are shown in Fig. 5(a) by squares and circles, respectively. The accuracy of these displacements is of ± 1 pixel, which, according to our optical magnification, corresponds to $\pm 11 \mu\text{m}$. The main α sequence represented in Fig. 3 yields the cycles ABCDE for both Δx_l (full red squares) and Δx_r (full blue circles) as shown in Fig. 5(a). The entry paths, OA, to the cycles are shown by hollow black squares and circles, respectively. Analogous considerations apply for θ_l and θ_r in Fig. 5(b). Note that only the path OA is similar to the experiments reported in Sec. 3.B of [17], where no detailed description of the footprint shape was provided.

Consequently, by considering α as a varying parameter, we are able to construct the contact-angle-hysteresis cycles, as shown in Fig. 6. Clearly, this cycle has similar properties to

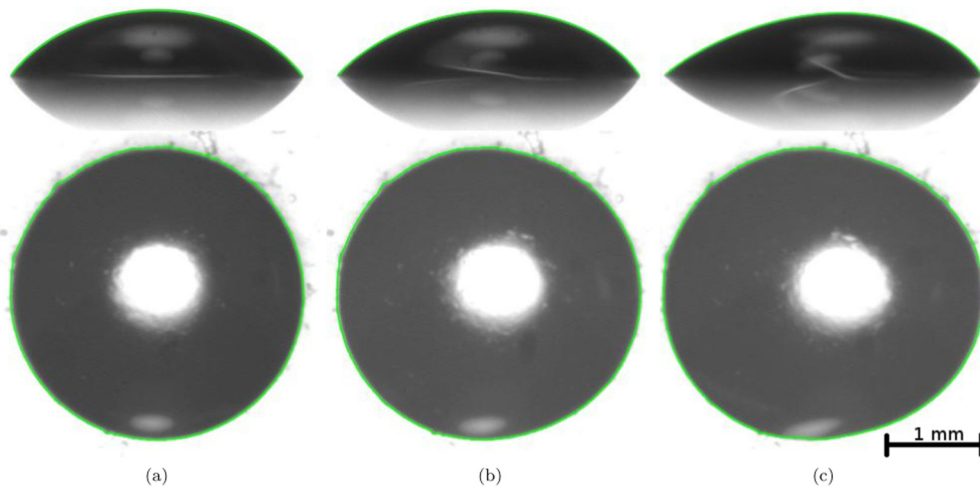


FIG. 4. Images as obtained from the goniometer of the side (top line) and top (bottom line) views of the drop for three inclination angles, α . (a) $\alpha = 0^\circ$, (b) $\alpha = 12.5^\circ$, and (c) $\alpha = 25^\circ$. The green lines are the contours extracted from the image analysis. The bar in (c) gives the scale of all pictures.

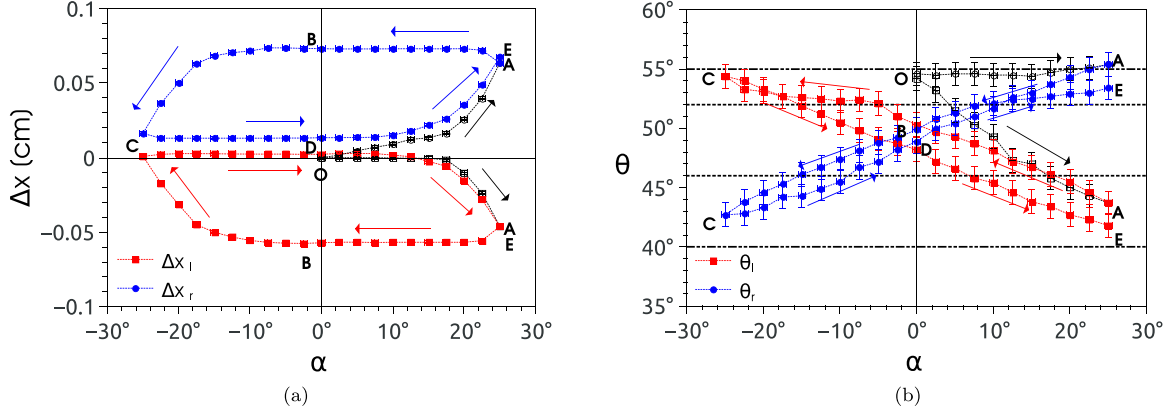


FIG. 5. Maximum plane inclination $\alpha_{\max} = 25^\circ$ and initial contact angle $\theta_0 = 55^\circ$: (a) Contact line displacements Δx_l and Δx_r (with respect to their positions at $\alpha = 0^\circ$) vs α . (b) Contact angles θ_l and θ_r vs α . The horizontal dotted (dot-dashed) lines in (b) correspond to $\theta_{\text{rcd}} = 46^\circ$ and $\theta_{\text{adv}} = 52^\circ$ ($\theta_{\text{min}} = 40^\circ$ and $\theta_{\text{max}} = 55^\circ$). The drop volume is $V = 0.657a^3 = 2.17 \text{ mm}^3$.

those described for the one depicted in Fig. 2, which uses the drop volume V as a varying parameter. Moreover, the values of the angles limiting the pinning and depinning regions are coincident with those in [24], where the same kind of substrate and fluid were used.

Equivalent cycles are also obtained for smaller $\theta_0 = 48^\circ$ and the same α_{\max} as in Fig. 6, i.e., for $\theta_0 < \theta_{\text{adv}}$ [see Fig. 7(a)]. The Δx range of the cycles decreases significantly (from ≈ 0.06 to ≈ 0.01 cm), but the θ range is only slightly smaller and scarcely out of the pinning interval ($\theta_{\text{rcd}}, \theta_{\text{adv}}$). This is because the equilibrium drop states along the OA branch can be reached just by increasing (decreasing) θ_r (θ_l) as α increases without the need to displace the contact line. These behaviors are similar to those shown in Sec. 3.C of [17]. In fact, the displacements occur after θ_r (θ_l) has approached θ_{adv} (θ_{rcd}), i.e., when the contact angles reach the boundaries of the pinning interval ($\theta_{\text{rcd}}, \theta_{\text{adv}}$). This description, based on θ versus Δx , is quite general and has the advantage that it avoids the dependence on α , in contrast to the analysis of the experimental results performed in [4]. Note that the value of α at which θ_r reaches θ_{adv} (namely, α_m in [4]) is not independent of θ_0 . Moreover, the numerical results in [18] show that α_l

($=\alpha_m$ in [4]) depends not only on θ_0 but also on the drop volume, V .

In Fig. 7(b), we keep the same initial condition as in Fig. 6 and reduce the value of α_{\max} to 15° . We observe that $\Delta x_r > 0$ only along the initial branch OA, while the cycles show variations of both θ_r and θ_l with $\Delta x_r = \Delta x_l = 0$, i.e., with pinned contact lines. The reason for this behavior is that for such small α , all the equilibrium states can be reached for θ_r and θ_l greater than θ_{rcd} , without the need to displace the contact lines.

A. Branch 1: From $\alpha = 0$ to 25° (O \rightarrow A with $\alpha_{\max} = 25^\circ$ and $\theta_0 = 55^\circ$)

As α increases from 0° to 25° we observe that the downhill contact point, x_r , displaces downward a bit more than the uphill one, x_l [see Fig. 5(a), O \rightarrow A for both Δx 's]. Concomitantly, the downhill contact angle approaches θ_{max} and remains practically constant until point A, while the uphill contact angle, θ_l , significantly diminishes, surpassing θ_{rcd} and approaching θ_{min} [see Fig. 5(b)]. These facts indicate that $\alpha = 25^\circ$ is very close to the limiting angle, α_{crit} , beyond which the drop would not remain at rest and would instead slide down the plane.

The experimental thickness profiles shown in Fig. 8(a) indicate that the drop width, w_x , increases while the maximum thickness decreases as the plane becomes more inclined. The footprints at points O, A, and an intermediate point $\alpha = 12.5^\circ$ are displaced to coincide at their leftmost point and compared in Fig. 8(b). Note that the footprints shapes are distorted from a circle only in the frontal part, i.e., for $x > w_x/2$, where they become more elongated. Interestingly, the maximum transversal width of the footprints, w_y , remains constant for all α 's. In the Appendix, we compare some of our measurements with other authors' data.

B. Branches 2, 3, and 4

As the plane is reverted to the horizontal position, the drop does not recover the same shapes for a given α in different branches due to the hysteresis of the contact angle.

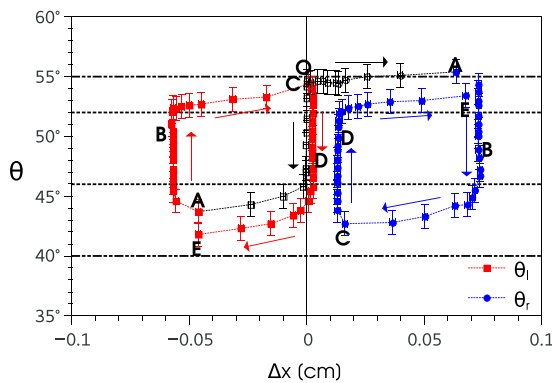


FIG. 6. Contact angles, θ_l and θ_r , vs contact line displacements, Δx_l and Δx_r , for $\alpha_{\max} = 25^\circ$ and $\theta_0 = 55^\circ$ for the drop in Fig. 5. The horizontal dotted (dot-dashed) lines correspond to $\theta_{\text{rcd}} = 46^\circ$ and $\theta_{\text{adv}} = 52^\circ$ ($\theta_{\text{min}} = 40^\circ$ and $\theta_{\text{max}} = 55^\circ$).

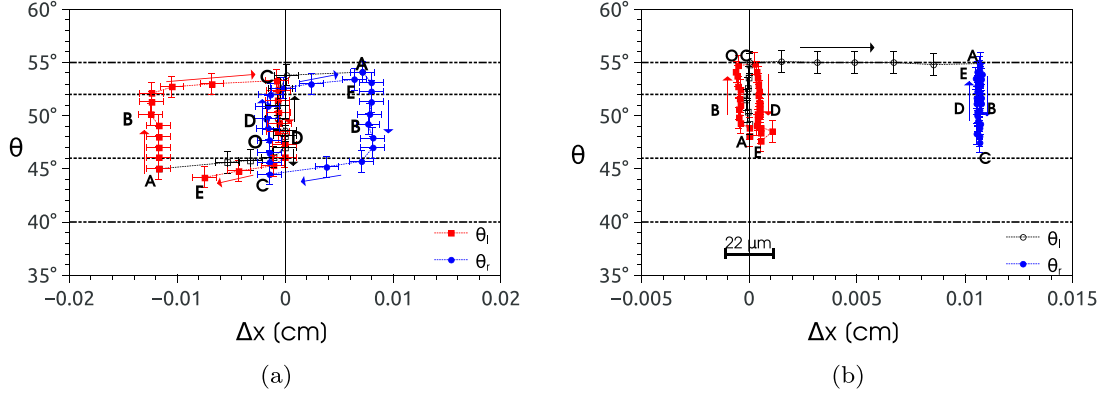


FIG. 7. Contact angles, θ_l and θ_r , vs contact line displacements, Δx_l and Δx_r , for (a) $\alpha_{\max} = 25^\circ$ and $\theta_0 = 48^\circ$ ($V = 0.474a^3 = 1.57 \text{ mm}^3$). (b) $\alpha_{\max} = 15^\circ$ and $\theta_0 = 55^\circ$ ($V = 0.519a^3 = 1.72 \text{ mm}^3$). The horizontal segment in (b) corresponds to the error bar for Δx .

For instance, for $\alpha = 12.5^\circ$ only the position x_l is almost coincident when comparing branches 1 and 2, but all other parameters differ. The effects for the thickness profiles and footprints with the same α are shown in Fig. 9.

We also verify that the profiles as well as the footprints depend not only on α but also on the direction in which α is changing, i.e., whether it is increasing or decreasing. In fact, we observe that the profiles for $\alpha = 12.5^\circ$ for branches 1 ($\alpha > 0$) and 3 ($\alpha < 0$) coincide when $|\alpha|$ is increasing (not shown for brevity). Those for branches 2 ($\alpha > 0$) and 4 ($\alpha < 0$) are identical when $|\alpha|$ is decreasing. This confirms the fact that (as expected) the sign of α is irrelevant.

Figure 10(a) compares the profiles for $\alpha = 0$ at points O, B, and D, where the drop has been affected by both positive and negative inclination angles. Clearly, the profiles at B and D do not coincide with that at O, but those at B and D are coincident if they are shifted to the left and right, respectively, until both maxima are at $x = 0$ [see Fig. 10(b)]. This fact implies that the effect of changing the sign of α only has the effect of exchanging the roles of the points x_l and x_r , which is a reasonable result. Therefore, this experimental verification reinforces the confidence in the validity of our measurements.

III. DROP SHAPE

One main observation of the experiments reported in Sec. II, as well as in the literature (see, e.g., [1,3,5]), is that the shape of the footprint does not remain circular for $\alpha > 0$. However, since most of the analytical approaches are restricted to small values of α , those studies have considered a circular shape for the footprint [15,25]. Instead, we will extend now our previous theory for noncircular footprints on horizontal planes [26] to inclined ones. In particular, we will adapt the polar coordinate formalism to the present case.

The governing equation for the thickness profile of the static drop can be obtained by considering the balance between the capillary pressure and both components of the gravitational force. In dimensionless form, we have

$$-\kappa + h \cos \alpha - x \sin \alpha = P = \text{const}, \quad (1)$$

where the thickness $h(x, y)$ and the spatial coordinates (x, y) are in units of $a = \sqrt{\gamma/(\rho g)}$ (the capillary distance), and P is the drop pressure in units of γ/a . Here, $\kappa = \nabla \cdot \mathbf{n}$ is the curvature of the drop free surface with normal vector

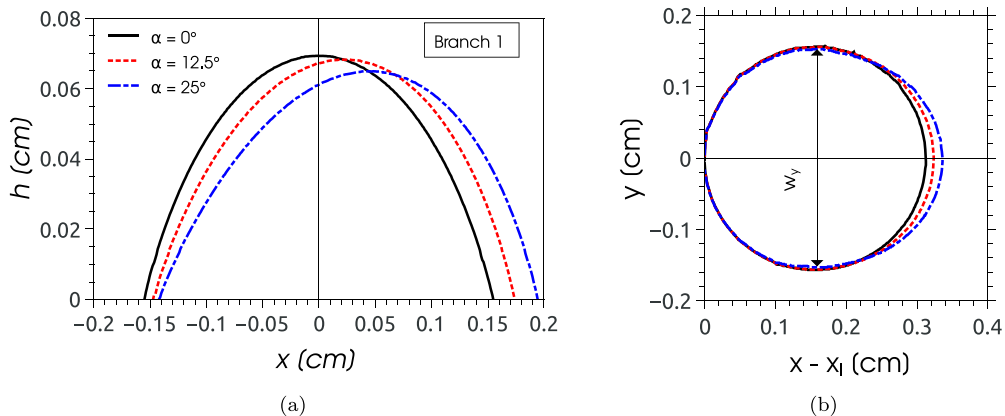


FIG. 8. Branch 1: (a) Thickness profiles at $\alpha = 0^\circ$ (solid lines), 12.5° (dashed lines), and 25° (dot-dashed line). (b) Corresponding footprints shifted so that the leftmost points are coincident. The drop volume is $V = 0.876a^3 = 2.9 \text{ mm}^3$.

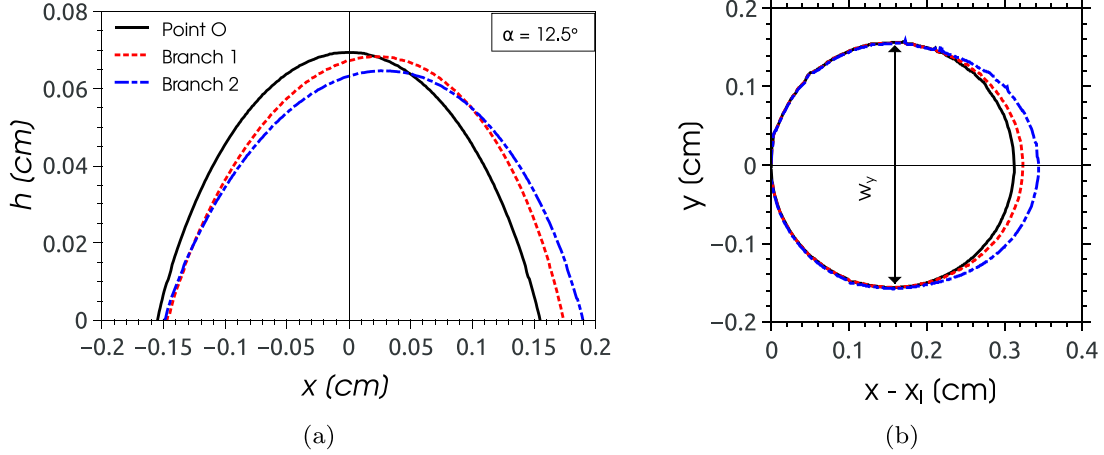


FIG. 9. Thickness profiles for $\alpha = 12.5^\circ$ at branch 1 (dashed line) and branch 2 (dot-dashed lines). The solid line corresponds to point O at $\alpha = 0$ and it is shown for comparison. (b) Corresponding footprints shifted so that the leftmost points are coincident.

$\mathbf{n} = \nabla F / |\nabla F|$, where $F = z - h(x, y) = 0$. Thus, we have

$$-\nabla \cdot \left(\frac{\nabla h}{\sqrt{1 + \epsilon |\nabla h|^2}} \right) + h \cos \alpha - x \sin \alpha = P = \text{const.} \quad (2)$$

For $\epsilon = 1$, the first term stands for the full surface curvature, while for $\epsilon = 0$ it yields the curvature valid only for small free surface slopes, i.e., $|\nabla h|^2 \ll 1$, in the context of the long-wave theory (lubrication approximation). The solution domain is the drop footprint, whose border line is denoted by a closed curve $\Gamma_\alpha(x, y) = 0$, where $h = 0$ for a given α . The determination of the constant P and the footprint shape, $\Gamma_\alpha(x, y) = 0$, depends on the approach used to solve Eq. (2).

To simplify this equation, we assume the validity of the lubrication approximation, even if the drops considered here do not have small contact angles. Thus, Eq. (2) with $\epsilon = 0$ reads (see, e.g., [27])

$$-\nabla^2 h + h \cos \alpha - x \sin \alpha = P, \quad (3)$$

which is a linear equation, similar to that studied in [26]. In fact, its solution can be written in the form

$$h = h_1 + \frac{P}{\cos \alpha} + x \tan \alpha, \quad (4)$$

where h_1 satisfies the homogeneous equation

$$\nabla^2 h_1 - h_1 \cos \alpha = 0. \quad (5)$$

To obtain h_1 , it is convenient to define the polar coordinates

$$r = \sqrt{x^2 + y^2}, \quad \varphi = \arctan \frac{y}{x}, \quad (6)$$

where the x origin is defined at the x coordinate of the point on $\Gamma_\alpha(x, y)$ with maximum y . Thus, this point corresponds to $(0, w_y/2)$, where w_y is the drop width in the transverse direction. Within this reference frame, we assume a factorized solution of Eq. (5) as $h_1 = R(r)\Phi(\varphi)$, and we find

$$h(r, \varphi) = \frac{P}{\cos \alpha} + r \cos \varphi \tan \alpha + \sum_{m=0}^{\infty} (A_m \cos m\varphi + B_m \sin m\varphi) I_m(r), \quad (7)$$

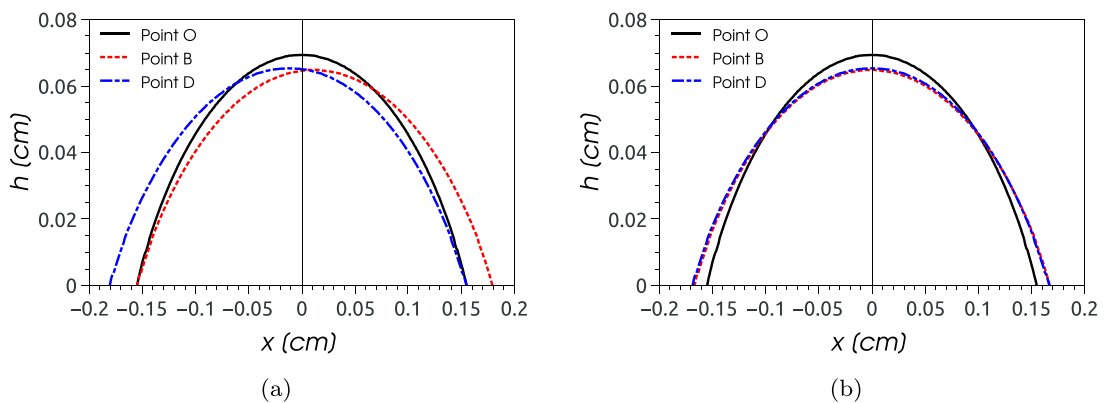


FIG. 10. (a) Thickness profiles for $\alpha = 0^\circ$ at different extreme points of the cycle: Solid line at start (point O), dashed line at the end of branch 2 (point B), and dot-dashed line at the end of branch 4 (point D). (b) Thickness profiles in (a) shifted toward left and right, respectively, until both maxima are at $x = 0$.

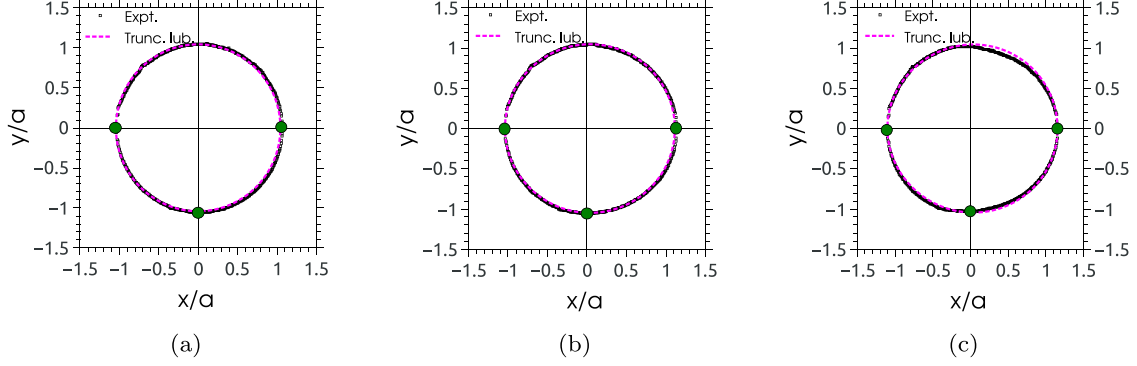


FIG. 11. Comparison between the experimental footprint (symbols) and those predicted by the truncated approximation, Eq. (8) (dashed line), when using only the positions of the three points indicated by the green dots (and the experimental value θ_r) for (a) $\alpha = 0^\circ$, (b) $\alpha = 12.5^\circ$, and (c) $\alpha = 25^\circ$.

where $I_m(r)$ are the modified Bessel functions of the first kind. Since the solution must be symmetric with respect to the x axis, we have $B_m = 0$ for all m , and then the problem reduces to finding the remaining constants A_m . In principle, this could be accomplished by setting $h = 0$ at an infinite number of points along the footprint border, $\Gamma_\alpha(x, y) = 0$.

To look for a useful analytical solution of Eq. (3), we further assume that the shape of the drop can be reasonably estimated by the first three terms of the series in Eq. (7), so that

$$h(r, \varphi) \approx h_{\text{trunc}}(r, \varphi) = \frac{P}{\cos \alpha} + r \tan \alpha \cos \varphi + A_0 I_0(r) + A_1 I_1(r) \cos \varphi + A_2 I_2(r) \cos 2\varphi. \quad (8)$$

The advantage of this approach is that the determination of the three constants A_i ($i = 0, 1, 2$) requires us to consider only three points at the footprint border. Note that the whole contact line is necessary to determine all the series coefficients, but we do not need such detailed information for the truncated solution. Here, we choose the points $(x = x_l, y = 0)$, $(x = x_r, y = 0)$, and $(x = 0, y = w_y/2)$, whose values are given as experimental data. Thus, we write the three conditions in polar coordinates as

$$\begin{aligned} h_{\text{trunc}}(r = r_l, \varphi = \pi) &= h_{\text{trunc}}(r = r_r, \varphi = 0) \\ &= h_{\text{trunc}}(r = w_y/2, \varphi = -\pi/2) = 0, \end{aligned} \quad (9)$$

where $r_l = -x_l$ and $r_r = x_r$.

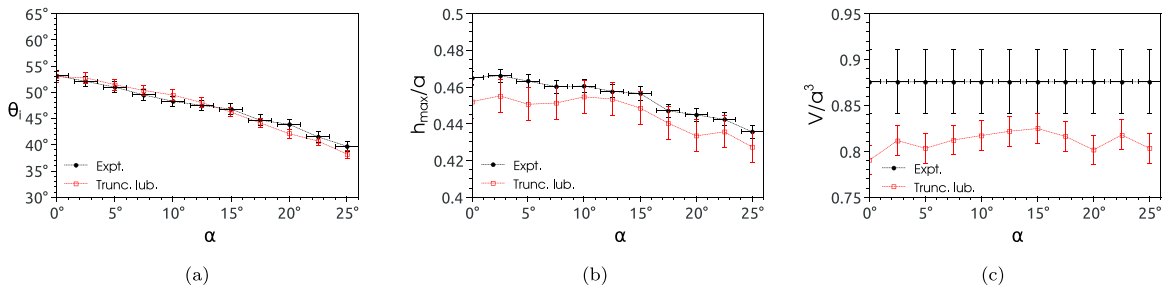


FIG. 12. Comparison between the predictions of h_{trunc} and the experimental data for (a) the contact angle at the left, (b) the maximum drop thickness, and (c) the drop volume.

The determination of the constant P is done by considering the contact angle at x_r as a known (measured) quantity, i.e., θ_r . Thus, we have the additional condition

$$\theta_r = - \left. \frac{\partial h_{\text{trunc}}}{\partial r} \right|_{(r_r, 0)}. \quad (10)$$

Finally, when all three constants A_i and P have been calculated, the predicted footprint shape is obtained by the implicit equation $h_{\text{trunc}}(r, \varphi) = 0$. Figure 11 shows comparisons of theoretical footprints (dashed lines) with experimental data (symbols). For both $\alpha = 0^\circ$ and 12.5° , the predicted footprints as given by Eq. (8) are very close to the experimental data within the measurement error. Only a slight difference is observed on the right side for $\alpha = 25^\circ$. Therefore, we can say that there is a remarkable agreement with the experimental footprints.

The truncated solution is able to yield other parameters, such as θ_l , h_{max} , and V . For the contact angle, θ_l , we use the expression

$$\theta_l = \left. \frac{\partial h_{\text{trunc}}}{\partial r} \right|_{(r_l, \pi)}, \quad (11)$$

which leads to a very good agreement with the measured data [see Fig. 12(a)]. The maximum thickness, h_{max} , also agrees with the experiments within the experimental error bars [see Fig. 12(b)]. Note that the predicted drop volume, V , is at most 9% smaller than the experimental value [see Fig. 12(c)].

The knowledge of azimuthal distribution of the contact angle, $\theta(\varphi)$, has been the object of several previous works [15,25]. Only the contact angles at the points $(x_l, 0)$ and $(x_r, 0)$

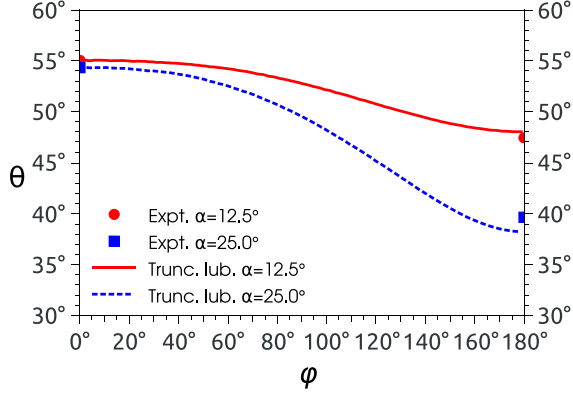


FIG. 13. Azimuthal distribution of contact angle, θ , as given by the truncated solution for $\alpha = 12.5^\circ$ (red solid line, $Bo = 1.01$) and $\alpha = 25^\circ$ (blue dashed line, $Bo = 2.15$). The symbols at $\varphi = 0^\circ$ and 180° stand for the experimental data, namely θ_l and θ_r for $\alpha = 12.5^\circ$ (red circles) and $\alpha = 25^\circ$ (blue squares).

of the $h(x, 0)$ profile are usually reported in the experiments, except for [25], where θ was measured at eight different azimuthal angles. Other authors have performed numerical simulations to obtain $\theta(\varphi)$. Some have assumed a circular shape for the footprint [12,13] and others have used noncircular shapes obtained by minimization of the required hysteresis range [28]. In general, all the functions $\theta(\varphi)$ show a smooth variation between θ_r and θ_l [11], except that in [28], which resembles a step function with a linear transition region.

Our analytical solution can provide the full azimuthal distribution of the contact angle, $\theta(\varphi)$. To do so, we consider the z component of the normal vector to the free surface, and we obtain

$$n_z = \cos \theta(r(\varphi), \varphi) = \left[1 + \left(\frac{\partial h}{\partial r} \right)^2 + \left(\frac{1}{r} \frac{\partial h}{\partial \varphi} \right)^2 \right]^{-1/2} \quad (12)$$

$\epsilon = 1,$

where $r(\varphi)$ is the footprint boundary given by $\Gamma_\alpha(r, \varphi) = 0$. Within the long-wave approximation, we consider this

equation for $\cos \theta \approx 1 - \theta^2/2$, and thus we find

$$\theta(r(\varphi), \varphi) = \pm \sqrt{\left(\frac{\partial h}{\partial r} \right)^2 + \left(\frac{1}{r} \frac{\partial h}{\partial \varphi} \right)^2}, \quad \epsilon = 0. \quad (13)$$

Then, $\theta(\varphi)$ is obtained by plugging Eq. (8) into Eq. (13) with the calculated values of the constants A_i and P . The predicted distributions for $\alpha = 12.5^\circ$ and 25° are shown in Fig. 13(a). Note that we are able to predict $\theta(\varphi)$ from the sole knowledge of θ_r (symbols at $\varphi = 0^\circ$). Moreover, the theoretical results for θ_l are in reasonable agreement with the experimental data (symbols at $\varphi = 180^\circ$). For $0 < \varphi < \pi$, we observe that the size of the footprint region facing downhill ($|\varphi| \approx 0$, in which $\theta \approx \theta_r$) increases, and that the transition from θ_l to θ_r becomes more abrupt as α increases.

The theoretical studies reported in the literature [15,16] are limited to a small Bond number, which is defined as

$$Bo = \frac{w_x^2}{a^2} \sin \alpha. \quad (14)$$

Thus, their validity is limited to either small α or small drop diameter, or both. Instead, the truncated solution presented here allows us to obtain $\theta(\varphi)$ without any restriction on the value of the Bond number.

IV. SUMMARY AND CONCLUSIONS

In this paper, we report measurements of the contact-angle-hysteresis curves and the possible equilibrium states by using the plane inclination, α , up to near a maximum value beyond which the drop starts sliding down. The results are compared with those of usual hysteresis cycles obtained by varying the drop volume, V , instead. The experiments show that both methods yield hysteresis cycles with the same contact-angle intervals, a fact confirming that they are an intrinsic consequence of the wetting properties of the system.

While the drop footprint remains circular in the varying volume method, the varying plane inclination method generates equilibrium drops with noncircular footprints. This might seem like a drawback of the method at first glance, but it provides interesting detailed insight into alternative

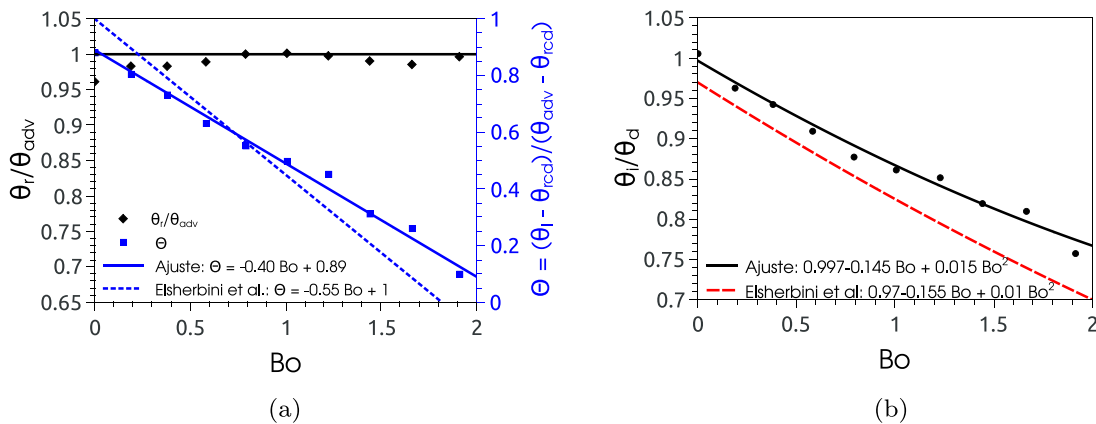


FIG. 14. Contact angles as functions of Bond number, Bo , along branch 1: (a) θ_r/θ_{\max} (diamonds) and the relative deviation of θ : $\Theta = (\theta_l - \theta_{\min})/(\theta_{\max} - \theta_{\min})$ (squares). The thick solid line is the best quadratic fit of the squares. (b) Experimental data and best quadratic fit for the ratio of both contact angles θ_l/θ_r . The dashed line corresponds to [25].

equilibrium drop shapes that are reached taking into account the hysteresis cycle. In particular, we observe that the most important changes with respect to the initially circular footprint for $\alpha = 0$ occur in the downhill region [see, e.g., Fig. 8(b)]. However, these deformations are not the same at different parts of the cycle, even though they correspond to equal α [see Fig. 9(b)]. On the other hand, the present experimental results have been compared successfully with previously reported data (see Fig. 14).

To describe the drop shape (both free surface and footprint) at different inclination angles, we have solved the pressure equilibrium equation within the approximation of small contact angles. We prove that a truncated expression of the analytical solution suffices to determine both the free surface and the full footprint from a very small set of data at the footprint, namely the positions of three points on the curve, and a contact angle at one of them. Our theoretical solution has a practical use, since two of those points as well as the contact angle are easily measured from the lateral view of the drop, which is the usual setup in most of the experiments reported in the literature. The third point can be extracted from a knowledge of the transverse width of the drop.

The contact-angle variation around the drop periphery, $\theta(\varphi)$, is another important characteristic of the drop shape that can be extracted from the theoretical analysis presented here. We should note that this angular information is very difficult to measure, especially for an inclined plane. The implementation of a refractive technique similar to that used in [26,29], which yields θ all along the drop periphery, is left for future work. To the best of our knowledge, theoretical models have been developed in the literature only for small inclinations and small drop volumes, when the footprint can be considered circular. We obtain $\theta(\varphi)$ from the theoretical solution as a truncated series without these restrictions. When this solution is applied by using the measured value of θ_r ($\varphi = 0$), a very good prediction of θ_l ($\varphi = \pi$) is obtained. Unfortunately, comparisons of $\theta(\varphi)$ with experimental data at other values of φ are not possible, since these measurements have not yet been reported. In summary, we develop an alternative method to measure the static hysteresis cycle that yields nontrivial equilibrium drop shapes, whose main features have been studied here.

ACKNOWLEDGMENTS

I.C. and P.R. acknowledge postgraduate student fellowships from Consejo Nacional de Investigaciones Científicas y Técnicas (CONICET, Argentina). J.D. and A.G. acknowledge support from Agencia Nacional de Promoción Científica y Tecnológica (ANPCyT, Argentina) with Grant No. PICT 1067/2016.

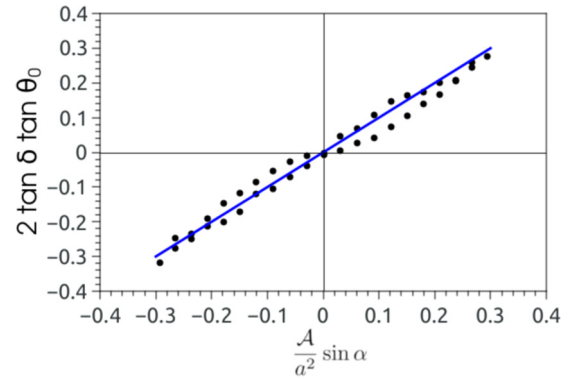


FIG. 15. Experimental data plotted in terms of the left- and right-hand sides of Eq. (A1) compared with the identity line.

APPENDIX: COMPARISON WITH PREVIOUS STUDIES

Our experimental data for branch 1 can be compared with those reported in the literature. To do that, we parametrize the effects of the component of gravity along the plane in terms of the Bond number, Bo [see Eq. (14)]. For instance, Fig. 14(a) shows that the ratio θ_r/θ_{\max} (diamonds) remains very close to unity as the plane is inclined. This result is in agreement with previously reported experimental [22,25] and numerical [17] results. Analogously to what was done in [25], we plot θ_l versus Bo by considering its relative deviation from θ_{\min} as $\Theta = (\theta_l - \theta_{\min})/(\theta_{\max} - \theta_{\min})$. Similarly to what was reported in [25], we also find a linear dependence for this relationship. Slope differences are a consequence of dealing with different liquid-substrate combinations. In Fig. 14(b) we show the ratio θ_l/θ_r versus Bo and obtain a quadratic fitting function (thick solid line). Interestingly, this curve is similar to that reported in [25] for other combinations of liquids and surfaces (see the dashed line and formulas in the figure).

When we consider the area of the thickness profile, \mathcal{A} , all along the cycle, we find that it remains practically constant with a value $\mathcal{A} = (0.694 \pm 0.007)a^2$. This allows us to compare this result with the predictions for a two-dimensional drop [7], i.e., for the problem of an infinitely long filament placed transversal to the incline. For instance, in [27] we find the following relationship between \mathcal{A} and the contact angles:

$$2 \tan \delta \tan \theta_0 = \frac{\mathcal{A}}{a^2} \sin \alpha, \quad (\text{A1})$$

where $\delta = (\theta_r - \theta_l)/2$ and $\theta_0 = (\theta_r + \theta_l)/2$. To compare this prediction with the present experiments, we plot the left-hand side of Eq. (A1) as obtained from the measured contact angles versus its right-hand side considering the measured values of \mathcal{A} (see the symbols in Fig. 15). The good agreement with the identity line [representing Eq. (A1)] shows that this formulation is still valid for three-dimensional drops such as those studied in this work.

[1] E. B. Dussan V., On the ability of drops or bubbles to stick to non-horizontal surfaces of solids. Part 2: Small drops or bubbles

having contact angles of arbitrary size, *J. Fluid Mech.* **151**, 1 (1985).

- [2] D. Quéré, Drops at rest on a tilted plane, *Langmuir* **14**, 2213 (1998).
- [3] E. Pierce, F. J. Carmona, and A. Amirfazli, Understanding of sliding and contact angle results in tilted plate experiments, *Colloids Surf., A* **323**, 73 (2008).
- [4] N. Janardan and M. V. Panchagnula, Effect of the initial conditions on the onset of motion in sessile drops on tilted plates, *Colloids Surf., A* **456**, 238 (2014).
- [5] C. W. Extrand and A. N. Gent, Retention of liquid drops by solid surfaces, *J. Colloid. Interface Sci.* **138**, 431 (1990).
- [6] C. W. Extrand and Y. Kumagai, Liquid drops on an incline: The relation between contact angles, drop shape, and retentive force, *J. Colloid. Interface Sci.* **170**, 515 (1995).
- [7] B. Krasovitski and A. Marmur, Drops down the hill: Theoretical study of limiting contact angles and the hysteresis range on a tilted plate, *Langmuir* **21**, 3881 (2005).
- [8] A. I. El Sherbini and A. M. Jacobi, Retention forces and contact angles for critical liquid drops on non-horizontal surfaces, *J. Colloid Interface Sci.* **299**, 841 (2006).
- [9] N. Gao, F. Geyer, D. W. Pilat, S. Wooh, D. Vollmer, H.-J. Butt, and R. Berger, How drops start sliding over solid surfaces, *Nat. Phys.* **14**, 191 (2018).
- [10] N. Legrand, A. Daerr, and L. Limat, Shape and motion of drops sliding down an inclined plane, *J. Fluid Mech.* **541**, 293 (2005).
- [11] S. R. Annapragada, J. Y. Murthy, and S. V. Garimella, Prediction of droplet dynamics on an incline, *Int. J. Heat Mass Transf.* **55**, 1466 (2012).
- [12] F. Milinazzo and M. Shinbrot, A numerical study of a drop on a vertical wall, *J. Colloid. Interface Sci.* **121**, 254 (1988).
- [13] R. A. Brown, F. M. Orr, and L. Scriven, Static drop on an inclined plate: Analysis by the finite element method, *J. Colloid Interface Sci.* **73**, 76 (1979).
- [14] V. M. Starov and M. G. Velarde, Surface forces and wetting phenomena, *J. Phys.: Condens. Matter* **21**, 464121 (2009).
- [15] J. De Coninck, F. Dunlop, and T. Huillet, Contact angles of a drop pinned on an incline, *Phys. Rev. E* **95**, 052805 (2017).
- [16] A. I. El Sherbini and A. M. Jacobi, Liquid drops on vertical and inclined surfaces II. A method for approximating drop shapes, *J. Colloid. Interface Sci.* **273**, 566 (2004).
- [17] T.-H. Chou, S.-J. Hong, Y.-J. Sheng, and H.-K. Tsao, Drops sitting on a tilted plate: Receding and advancing pinning, *Langmuir* **28**, 5158 (2012).
- [18] J. A. White, M. J. Santos, M. A. Rodríguez-Valverde, and S. Velasco, Numerical study of the most stable contact angle of drops on tilted surfaces, *Langmuir* **31**, 5326 (2015).
- [19] B. Xu, Z. Yuan, and Y. Wu, Simulation analysis on surface morphology and hysteresis characteristics of molten Sn–3.0Ag–0.5Cu sitting on the inclined Ni substrate, *Colloids Surf., A* **441**, 217 (2014).
- [20] A. K. Das and P. K. Das, Simulation of drop movement over an inclined surface using smoothed particle hydrodynamics, *Langmuir* **25**, 11459 (2009).
- [21] S. D. Iliev, Static drops on an inclined plane: Equilibrium modeling and numerical analysis, *J. Colloid Interface Sci.* **194**, 287 (1997).
- [22] V. Berejnov and R. E. Thorne, Effect of transient pinning on stability of drops sitting on an inclined plane, *Phys. Rev. E* **75**, 066308 (2007).
- [23] C. N. C. Lam, R. Wu, D. Li, M. L. Hair, and A. W. Neuman, Study of the advancing and receding contact angles: liquid sorption as a cause of contact angle hysteresis, *Adv. Colloid Interface Sci.* **96**, 169 (2002).
- [24] P. D. Ravazzoli, I. Cuellar, A. G. González, and J. A. Diez, Wetting and dewetting processes in the axial retraction of liquid filaments, *Phys. Rev. E* **95**, 053111 (2017).
- [25] A. I. El Sherbini and A. M. Jacobi, Liquid drops on vertical and inclined surfaces i. An experimental study of drop geometry, *J. Colloid. Interface Sci.* **273**, 556 (2004).
- [26] P. D. Ravazzoli, A. G. González, and J. A. Diez, Drops with non-circular footprints, *Phys. Fluids* **28**, 042104 (2016).
- [27] J. Diez, A. G. González, and L. Kondic, Instability of a transverse liquid rivulet on an inclined plane, *Phys. Fluids* **24**, 032104 (2012).
- [28] P. Dimitrakopoulos and J. J. Higdon, On the gravitational displacement of three-dimensional fluid droplets from inclined solid surfaces, *J. Fluid Mech.* **395**, 181 (1999).
- [29] A. G. González, J. Diez, R. Gratton, and J. Gomba, Rupture of a fluid strip under partial wetting conditions, *Europhys. Lett.* **77**, 44001 (2007).